RESEARCH ARTICLE

Editor's Choice

ADVANCED MATERIALS
www.advmat.de

Thorough Optimization for Intrinsically Stretchable Organic Photovoltaics

Xiangjun Zheng, Xiaoling Wu, Qiang Wu, Yunfei Han, Guanyu Ding, Yiming Wang, Yibo Kong, Tianyi Chen, Mengting Wang, Yiqing Zhang, Jingwei Xue, Weifei Fu, Qun Luo, Changqi Ma, Wei Ma, Lijian Zuo,* Minmin Shi,* and Hongzheng Chen**

The development of intrinsically stretchable organic photovoltaics (*is*-OPVs) with a high efficiency is of significance for practical application. However, their efficiencies lag far behind those of rigid or even flexible counterparts. To address this issue, an advanced top-illuminated OPV is designed and fabricated, which is intrinsically stretchable and has a high performance, through systematic optimizations from material to device. First, the stretchability of the active layer is largely increased by adding a low-elastic-modulus elastomer of styrene-ethylene-propylene-styrene tri-block copolymer (SEPS). Second, the stretchability and conductivity of the opaque electrode are enhanced by a conductive polymer/metal (denoted as M-PH1000@Ag) composite electrode strategy. Third, the optical and electrical properties of a sliver nanowire transparent electrode are improved by a solvent vapor annealing strategy. High-performance *is*-OPVs are successfully fabricated with a top-illuminated structure, which provides a record-high efficiency of 16.23%. Additionally, by incorporating 5–10% elastomer, a balance between the efficiency and stretchability of the *is*-OPVs is achieved. This study provides valuable insights into material and device optimizations for high-efficiency *is*-OPVs, with a low-cost production and excellent stretchability, which indicates a high potential for future applications of OPVs.

1. Introduction

Portable wearable devices have a high potential for applications in human health monitoring, human–computer interaction, and Internet of Things.[1,2] In addition to the basic functionality, the practical scenarios necessitate flexibility and even stretchability of wearable devices. This is crucial to overcome the inevitable deformation to fulfill the requirements of wearable power sources, e.g., ultra-flexibility, lightweight, high power density, and intrinsic stretchability.[3–7] Among the existing power supply technologies, organic photovoltaics (OPVs) emerge as most promising candidates to meet these requirements due to their intrinsic stretchability with intermolecular van der Waals interactions.[8,9] In recent years, there has been a significant progress in the development of OPVs.[10–25] The best certified power conversion efficiencies (PCEs) of single-junction and tandem OPVs have reached remarkable levels of 19.40% and 20.30%, respectively.[26,27] These state-of-the-art efficiency achievements indicate the high potential of OPVs for practical applications.[28,29] Therefore, OPVs are expected to have a unique role in wearable devices with the development of intrinsically stretchable OPVs (*is*-OPVs) becoming an essential element of OPV-based wearable devices.

However, the simultaneous provision of a high performance and good stretchability is a challenging task that requires a

X. Zheng, X. Wu, G. Ding, Y. Wang, Y. Kong, T. Chen, M. Wang, Y. Zhang, W. Fu, L. Zuo, M. Shi, H. Chen
State Key Laboratory of Silicon and Advanced Semiconductor Materials
International Research Center for X Polymers
Department of Polymer Science and Engineering
Zhejiang University
Hangzhou 310027, P. R. China
E-mail: zjuzlj@zju.edu.cn; minminshi@zju.edu.cn; hzchen@zju.edu.cn

Q. Wu, J. Xue, W. Ma
State Key Laboratory for Mechanical Behavior of Materials
Xi'an Jiaotong University
Xi'an 710049, P. R. China

Y. Han, Q. Luo, C. Ma
Printable Electronics Research Center
Suzhou Institute of Nano-Tech and Nano-Bionics
Chinese Academy of Sciences (CAS)
Suzhou 215123, P. R. China
E-mail: qluo2011@sinano.ac.cn

W. Fu, L. Zuo, H. Chen
Zhejiang University-Hangzhou Global Scientific and Technological Innovation Center
Hangzhou 310014, P. R. China

The ORCID identification number(s) for the author(s) of this article can be found under https://doi.org/10.1002/adma.202307280

DOI: 10.1002/adma.202307280

synergic optimization of various components, including substrates, opaque electrodes, transparent electrodes, active layer, and transport layer materials. The aim is to achieve stretchability without compromising the optoelectronic properties.[8] Among these factors, the development of stretchable active layers is the key to the development of *is*-OPVs. Generally, stretchable active layers can be achieved in two manners. One strategy involves design of the active layer materials with intrinsic stretchability, so that the original binary active layer system can achieve a better stretchability.[30–33] The other method involves a ternary strategy to introduce a third component to a binary system with weak tensile properties but high efficiency, e.g., donors, acceptors, or highly elastic polymers, to improve the stretchability of the active layer.[34–39] Recently, the latter method has been of interest as it does not require synthesis of new molecules and provides a higher generalizability. However, it is still challenging to balance the efficiency and stretchability. For example, addition of a small amount of the third component may not significantly impact the efficiency but only marginally improves tensile properties. On the other hand, addition of a large amount of the third component can largely enhance tensile properties but largely reduces the efficiency. Therefore, it is necessary to explore new molecules to balance the efficiency and stretchability of the active layer.

Another crucial aspect of the fabrication of *is*-OPVs is to develop stretchable electrodes. For opaque electrodes, liquid metals, e.g., eutectic gallium indium (EGaIn), are most commonly employed due to their superior ductility.[31–35,40] However, the EGaIn electrode suffer from a high surface tension accompanied by an instantaneous oxidation, which makes it unsuitable for an opaque bottom electrode. In general, common metals such as Ag are widely used as opaque top electrodes. Additionally, our previous study demonstrated that Ag as a bottom electrode in a top-illuminated device provides advantages in the fabrication of flexible and ultra-flexible devices, achieving a high efficiency of ≈17%.[3,4,41] However, the Ag-based *is*-OPVs usually exhibit a low tensile stability due to the limited stretchability of the Ag electrode.[39,42] Therefore, it is necessary to develop a new class of stretchable opaque electrodes for top-illuminated *is*-OPVs.

For the transparent electrodes, Ag nanowires (AgNWs) and conductive polymer PH1000 are extensively utilized due to their intrinsic stretchability. AgNWs are outstanding owing to their superior optical and electrical properties.[5,39,43–47] The spin coating method is commonly employed to prepare AgNW films for OPV transparent electrodes, a simple and widely employed approach. However, the shear force during the spin coating can lead to more aligned arrangements of AgNWs and potential aggregation issues, which may hinder the provision of excellent optical and electrical properties of AgNW electrodes. Therefore, more reliable and superior electrode materials, processing methods, and device structures are required to simultaneously reach high performances and superior mechanical properties for *is*-OPVs.

In this regard, in this study, we demonstrate top-illuminated OPVs with a good stretchability and high performance by delicately optimizing the material and device structures. First, the stretchability of the active layer is increased by adding a styrene-ethylene–propylene–styrene tri-block copolymer (SEPS) elastomer. The incorporation of less than 10% SEPS has a minimal impact on the crystallization behavior of the active layers and overall PV performances of the devices. Second, the stretchability and conductivity of the opaque electrode are enhanced by a conductive polymer/metal (M-PH1000@Ag) composite electrode strategy. M-PH1000 provides stretchability and forms a continuous conductive network, while the Ag layer improves the electrical conductivity and enhances the light utilization efficiency for a better device performance. Third, the optical and electrical properties of AgNW transparent electrodes are improved by solvent vapor annealing (SVA), achieved by precisely adjusting the surface tension of the substrate and dispersant for AgNWs. Moreover, through a thorough material-to-device optimization, we successfully fabricated OPVs on the stretchable substrates based on the top-illuminated structure, which exhibited a record-high efficiency of 16.23% and PCE retention rate of over 80% after 200 stretching cycles with a strain of 10%, which is the best value among *is*-OPVs.

2. Results and Discussion

2.1. Stretchable Active Layer

Figure 1a illustrates the top-illuminated structure employed in this study, with M-PH1000@Ag as an opaque electrode and AgNWs as a transparent electrode. We aimed to systematically optimize the photo-active layers and electrodes and reconstruct the device structure to achieve high-performance *is*-OPVs. Figure 1b shows the chemical structures of active layer materials, i.e., PM6, L8-BO, and BTP-eC9. The energy diagrams of various materials are shown in Figure S1 (Supporting Information). Among them, the binary PM6:L8-BO (1:1.2) blend with a conventional structure, shown in Figure S2 (Supporting Information), exhibits the best efficiency of 19.06%, with an open-circuit voltage (V_{OC}) of 0.89 V, short-circuit current density (J_{SC}) of 26.60 mA cm^{-2}, and fill factor (FF) of 80.77%, among the highest PCEs for PM6:L8-BO-based OPVs.[12,14,17] However, the high crystallinity of PM6 and L8-BO leads to a rather brittle active layer film, which is unfavorable for the development of high-performance stretchable OPV devices.

The introduction of materials with low elastic moduli into the active layer is an effective strategy to enhance its stretchability. Here, we incorporated an elastic polymer, SEPS (with a modulus of ≈2.3 MPa at 100%), as the third component into the PM6:L8-BO system to improve the stretchability. As shown in Figure 1c, due to the absence of crystalline units in the main chain, SEPS has superior elasticity and hysteresis behavior.[48] As shown in Figure 1d,e, to investigate the impact of different SEPS contents on the PV performances of PM6:L8-BO-based OPV devices, we analyzed the influences of 2%, 5%, 10%, and 20% SEPS. The device parameters are summarized in **Table 1** (Supporting Information). The addition of 2%, 5%, and 10% SEPS did not cause a large degradation of the device performance. The corresponding PCEs were 18.97%, 18.46%, and 17.96%, respectively. When the content of SEPS was further increased to 20%, the performance of the device decreased largely, with a PCE of 15.44%. To achieve a better device performance, we employed a ternary strategy by utilizing a PM6:L8-BO:BTP-eC9 (1:0.6:0.6) blend, known for its high efficiency in OPV active layers.[13] The ternary device exhibited the best efficiency of 19.26%. Subsequently, we assessed the influences of 5% and 10% SEPS on the performances of ternary devices, as shown in Figure S3 (Supporting Information). The

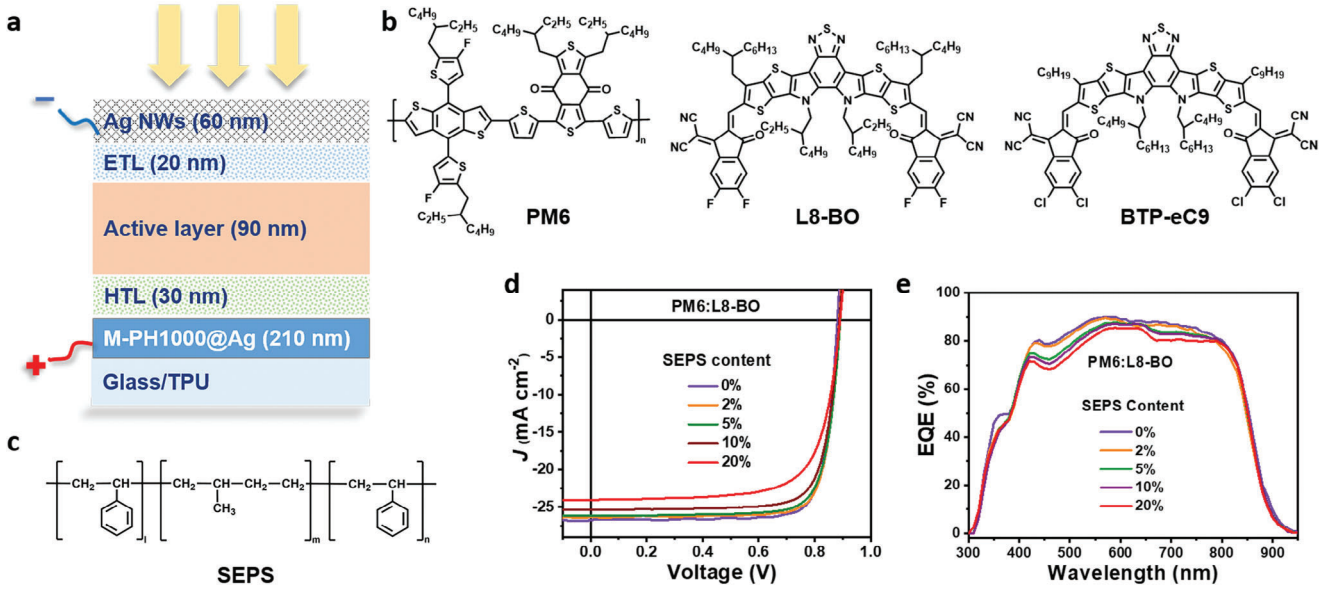

Figure 1. Basic characteristics of the designed top-illuminated *is*-OPVs. a) The device structure of rigid and *is*-OPVs. Chemical structures of the b) active layer (PM6, L8-BO and BTP-eC9) and c) elastomer polymer (SEPS). d) *J*–*V* characteristics and e) EQE spectra of ITO-based rigid binary (PM6:L8-BO) devices with different SEPS contents.

PCEs at contents of 5% and 10% were 18.89% and 18.28%, respectively, showing a similar trend to that of the PM6:L8-BO devices.

The addition of the third component can significantly impact the molecular packing, and thus affect the device performance. To investigate the effect of the addition of SEPS on the aggregation within the active layer, we conducted a grazing-incidence wide-angle X-ray scattering (GIWAXS) analysis. As shown in **Figure** 2a, in the in-plane direction, the positions of the L8-BO (100) and (200) peaks were constant at different SEPS contents. The (200) lamellar peak represents the skeleton (backbone) packing of PM6, which also remains at the same position regardless of the SEPS content. In the out-of-plane direction, the (010) π–π peaks of the active films were consistently around 1.75 Å^{-1}, indicating an unaffected π–π stacking. The crystallinity exhibited a slight change at SEPS contents below 10%, but decreased at 20%. The crystal coherence lengths of the π–π peaks were ≈18.5 Å. The longer-range π–π peaks were around 0.55 Å^{-1}. These results suggest that a low SEPS content does not disrupt the crystallization of L8-BO, while 20% SEPS negatively impacts the crystallization properties of the active blend films, leading to the decreased device performance.

Further, we investigated the miscibility among PM6, L8-BO, and SEPS. Water–diiodomethane (DIM) contact angle measurements were conducted on the corresponding films at room temperature to assess the surface energy, as shown in Figure S4 and Table S1 (Supporting Information). The surface energies of PM6, L8-BO, and SEPS were 34.83, 38.88, and 27.99 mN m^{-1}, respectively. The miscibility between PM6:L8-BO, PM6:SEPS, and L8-BO:SEPS can be quantified by the Flory-Huggins interaction parameter χ. The calculation results demonstrate that $\chi^{PM6-L8\text{-}BO}$ (0.111) < $\chi^{PM6-SEPS}$ (0.374) < $\chi^{L8\text{-}BO-SEPS}$ (0.893), which indicates that PM6 has a better miscibility with L8-BO, while SEPS tends to self-aggregate, as confirmed below.

To further confirm the state of SEPS in the active layer, we analyzed the surface and bulk morphologies of PM6:L8-BO films with different contents of SEPS by atomic force microscopy (AFM) and transmission electron microscopy (TEM). AFM height and phase images are shown in Figure 2b and

Table 1. Photovoltaic performances of the Rigid ITO-based devices. The ± refers to the standard deviation.

Active layer	SEPS content	V_{OC} [V]	J_{SC} [mA cm^{-2}]	$J_{ph,\,cal}$ [mA cm^{-2}]	*FF* [%]	PCE [%]
PM6:L8-BO	0%	0.89	26.60	26.21	80.77	19.06 (18.90±0.12)
	2%	0.89	26.43	26.05	80.74	18.97 (18.79±0.10)
	5%	0.89	25.96	25.42	79.71	18.46 (18.18±0.18)
	10%	0.89	25.49	25.05	79.01	17.96 (17.76±0.15)
	20%	0.89	24.04	23.91	71.80	15.44 (14.93±0.29)
PM6:L8-BO:BTP-eC9	0%	0.88	27.54	27.02	79.94	19.26 (19.15±0.08)
	5%	0.88	27.25	26.79	79.28	18.89 (18.70±0.12)
	10%	0.87	26.81	26.33	78.15	18.28 (18.12±0.11)

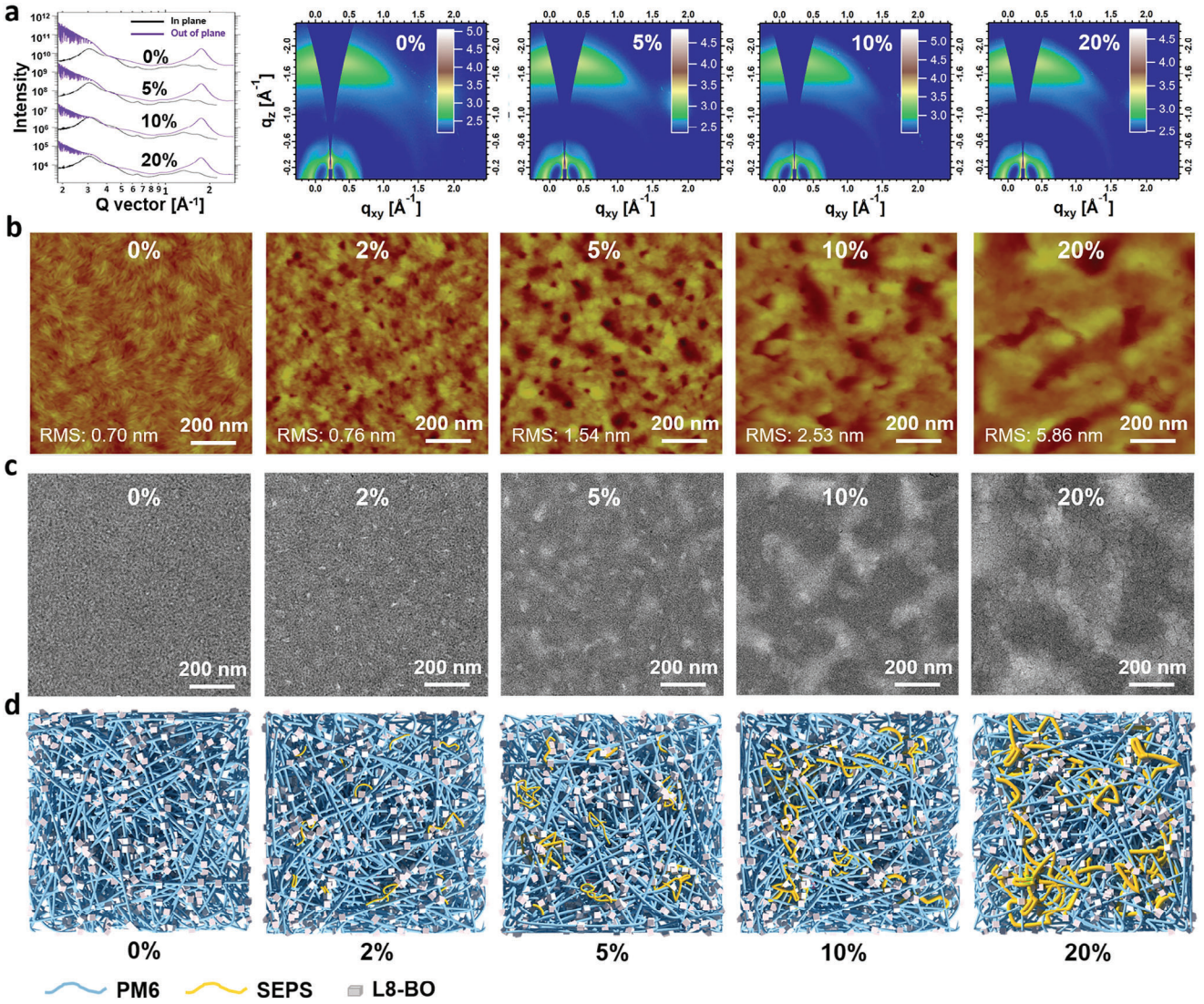

Figure 2. Morphologies of active layers with different SEPS contents. a) 1D X-ray profiles and 2D GIWAXS images of the PM6:L8-BO blend films with different SEPS contents. b) AFM height and c) TEM images of PM6:L8-BO blend films with different SEPS contents. d) The aggregation state model in the PM6:L8-BO blend films with different SEPS contents.

Figure S5 (Supporting Information). As the SEPS content increased, the roughness of the PM6:L8-BO film gradually increased, accompanied by an increase in dark areas. Considering the AFM images at a content of 0%, we speculate that these dark regions correspond to the self-aggregation of SEPS. The corresponding TEM images (Figure 2c), similar to the AFM images, show that the increase in the SEPS content caused changes in the internal morphology of the PM6:L8-BO films. Notably, at a SEPS content of 10%, distinct continuous phases were observed in the TEM images. Both AFM and TEM images revealed that SEPS tends to self-aggregate within PM6:L8-BO films. The degree of aggregation increased with the SEPS content. These conclusions are consistent with the above compatibility analysis.

Through the above analysis, we schemed an aggregation state model of different contents of SEPS in the PM6:L8-BO film, as shown in Figure 2d. In the binary film, there are uniformly dispersed small PM6:L8-BO blend domains, along with PM6 and L8-BO aggregation domains. When 2% SEPS is added, a slight aggregation occurs within the active layer. However, overall, it remains uniformly dispersed, which results in only a minor decrease in the device performance (PCE of 18.97%). With 5% SEPS, the degree of aggregation is increased, which leads to the formation of a small continuous structure in some areas. These structures slightly enhance the charge recombination, resulting in a slight decrease in device performance (PCE of 18.42%). With 10% SEPS, obvious aggregation and continuous structures appear in the active layer. However, these structures do not significantly affect the blend morphology of PM6:L8-BO, which leads to a marginal decrease in the device performance (PCE of 17.96%). When the SEPS content reaches 20%, a large number of aggregated and continuous structures are formed, even exceeding the thickness of the active layer film. These extensive, aggregated, and insulating SEPS domains largely reduce the device performance (PCE of 15.44%).

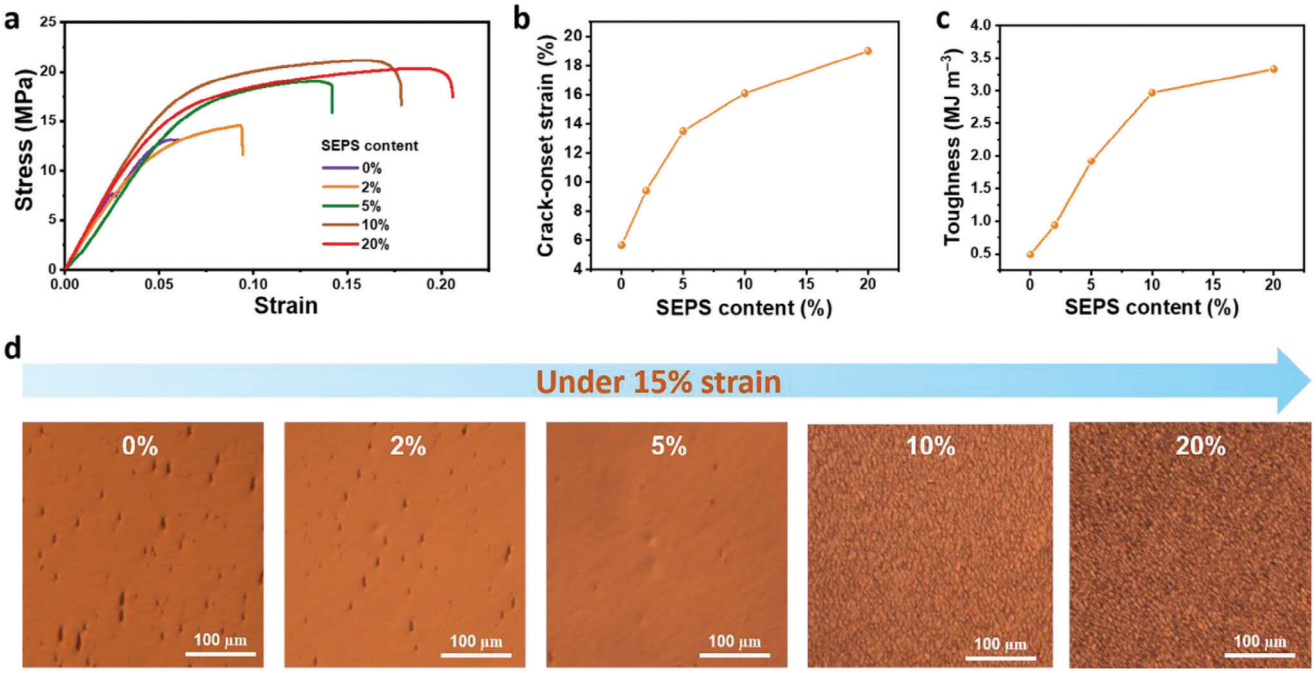

Figure 3. Stretchability of the active layer. a) Stress–strain curves of PM6:L8-BO blend films with different SEPS contents. b) COS and c) toughness of PM6:L8-BO blend films with different SEPS contents. d) Optical microscope images of PM6:L8-BO blend films with different SEPS contents at 15% strain.

The influence of different SEPS contents on the stretchability of the active layer was investigated by measuring the crack opening strain (COS) using the film-on-water method. As shown in **Figure** 3a–c and Table S2 (Supporting Information), the inclusion of SEPS significantly improved the stretchability and toughness, as indicated by the increased COS at a higher SEPS content. For the PM6:L8-BO blend films, the COSs were 5.67%, 9.41%, 13.5%, 16.1%, and 19.0% at SEPS contents of 0%, 2%, 5%, 10%, and 20%, respectively. The corresponding toughnesses were 0.49, 0.94, 1.92, 2.97, and 3.33 MJ m^{-3}, respectively. These findings reflect the effectiveness of the use of SEPS to enhance the stretchability of the active layer. Additionally, as shown in Figure S6 and Table S2 (Supporting Information), the efficiency stretchability factor (ESF = PCE × COS × 100 × 100%) was used to assess the efficiencies and mechanical performances of the blend films.[37] The ESFs for SEPS contents of 0%, 2%, 5%, 10%, and 20% were 1.08%, 1.78%, 2.48%, 2.89%, and 2.93%, respectively, which indicates a better balance between the stretchability and efficiency in devices with SEPS contents of 5–20% for the active layer. In addition, as shown in Figures S7–S10 and Table S3 (Supporting Information), we measured the stretchability of the ternary PM6:L8-BO:BTP-eC9 blend films with different SPES contents. They exhibited a similar trend to that of the binary PM6:L8-BO blend films.

Furthermore, as shown in Figure S11 (Supporting Information), optical microscopy images of the active layers with varying SEPS contents were obtained at different stretching strengths. The stretchability of the active layer is significantly enhanced with the increase in the SEPS content. We present optical microscopy images of active layers with different SEPS contents at a stretching strength of 15% (Figure 3d). The active layers with 0% and 2% SEPS cracked obviously at a stretching strength of 15% due to the lack of a continuous SEPS structure. Conversely, the film with 5% SEPS experienced minimal changes owing to the subtle continuity provided by the SEPS. Notably, when the SEPS contents were 10% and 20%, the continuous structure of a large number made the film more flexible, and thus the film exhibited a reversible deformation.

2.2. Stretchable Opaque Electrode

Another challenge in the fabrication of stretchable OPVs is to develop stretchable electrodes with a high conductivity, suitable work function, and simple fabrication process under light-tight conditions. Additionally, the electrode should exhibit certain reflective performance to form an optical chamber to maximize the light absorption. Based on the above analysis, we designed a new type of stretchable opaque electrode, denoted as M-PH1000@Ag, composed of a modified PH1000 (M-PH1000, 150 nm) and Ag (60 nm) layer. In the M-PH1000@Ag electrode, the conductive polymer M-PH1000 provides a good stretchability, which enables to form a continuous conductive network during stretching. Moreover, the sulfonate group of PSS and the sulfur elements in the conjugated structure of PEDOT can respectively generate O–Ag and S–Ag interaction forces with Ag. These forces can enhance the adhesion ability between M-PH1000 and Ag, thereby improving the flexibility of M-PH1000@Ag. Additionally, the deposition of Ag largely improves the electrical conductivity of the composite electrode, while the high reflectivity of Ag improves the light utilization efficiency of the active layer, which is beneficial to the improvement in device performance.

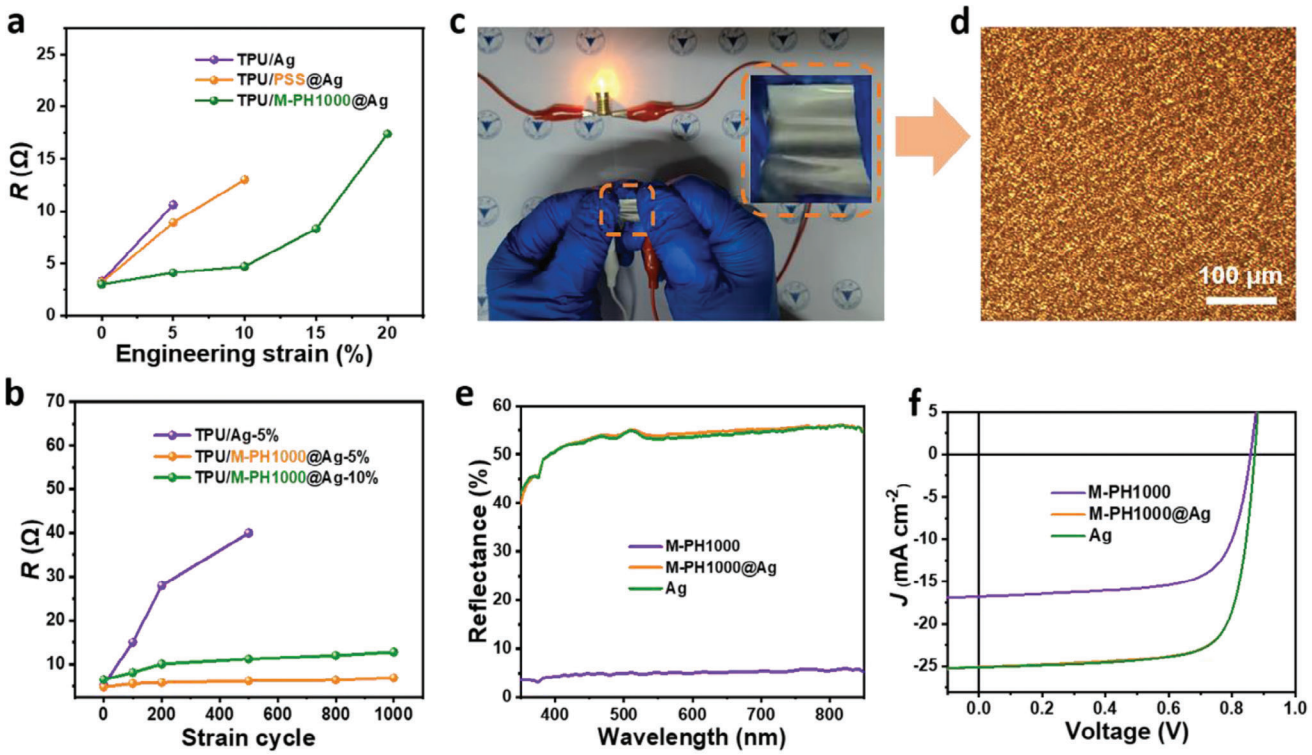

Figure 4. Stretchable opaque electrode. a) The resistance of TPU/Ag, TPU/PSS/Ag, and TPU/M-PH1000@Ag electrodes under different strains. b) The resistance of TPU/Ag, and TPU/M-PH1000@Ag electrodes under different strain times. c) The display of the conductivity of the M-PH1000@Ag electrode when stretching. d) The optical microscopy image of M-PH1000@Ag electrode under ≈20% strain. e) The reflectance of M-PH1000, M-PH1000@Ag, and Ag electrodes. f) The *J*–*V* curves of M-PH1000, M-PH1000@Ag, and Ag electrodes-based binary top-illuminated devices.

As shown in **Figure** 4a, we measured the resistance of electrodes with dimensions of 1.5 × 2.0 cm^2 under different strains. The Ag electrode on a thermoplastic urethane (TPU) substrate can endure stretching strengths up to 5%. A sharp increase in resistance (from 3.3 to 10.6 Ω) was observed due to the limited stretchability of the metal Ag electrode. The introduction of the stretchable polymer electrode (M-PH1000@Ag composite) improved the stretch-resistance performance. Even at a tensile strength of 10%, the M-PH1000@Ag electrode has an almost constant resistance (3.0 to 4.7 Ω). The substitution of M-PH1000 with the nonconductive poly(styrenesulfonate) (PSS) yields similar stretch-resistance properties, which validates the effectiveness of M-PH1000@Ag as a composite electrode. Additionally, as shown in Figure 4b, the resistance changes after the stretching-releasing cycles indicate that the Ag electrode's resistance increases significantly (4.3 to 40.0 Ω) after 500 cycles, while the M-PH1000@Ag electrode remains almost unaltered after 1000 cycles. Moreover, even with the increased tensile strength (10%), the M-PH1000@Ag electrode experiences a resistance increase from 6.5 to 12.8 Ω after 1000 cycles.

To clearly demonstrate the stretchability of the M-PH1000@Ag composite electrode, we conducted a visual demonstration of its conductivity under stretching. As shown in Figure 4c and Video S1 (Supporting Information), we connected the M-PH1000@Ag electrode to an external 6 V power supply, which powered a tungsten filament lamp. The resistance changes of the composite electrode during stretching were reflected in the brightness variations of the lamp. The M-PH1000@Ag electrode maintained its normal function even after multiple stretching cycles, while the Ag electrode failed after only two stretches. This reflects the superior stretchability of the M-PH1000@Ag composite electrode. Further, as shown in Figure 4d, we analyzed the morphology of the stretched M-PH1000@Ag electrode using optical microscopy. The stretching force caused dispersion of the Ag film into fine particles. At this stage, the conductive network mainly relied on M-PH1000, while the dispersed silver particles theoretically enhanced the conductivity of M-PH1000. Furthermore, we investigated the influences of the reflection performances of the M-PH1000, Ag, and M-PH1000@Ag electrodes on the top-illuminated device, considering their significant impact on the PV performance. In Figure 4e, both Ag and M-PH1000@Ag electrodes exhibited strong reflection capabilities in the range of 300–1000 nm. However, the M-PH1000 electrode exhibited high light transmission and absorption capabilities, resulting in a relatively low reflectivity.

Subsequently, we fabricated rigid top-illuminated OPV devices with a structure of glass/(Ag or M-PH1000@Ag)/PCP-2F-Li/PEDOT:PSS (Al4083)/PM6:L8-BO/ZnO nanoparticles (NPs)/AgNWs based on the corresponding electrodes. As shown in Figure 4f and Table S4 (Supporting Information), the PV performances of the devices based on Ag and M-PH1000@Ag electrodes do not significantly differ, with PCEs of 16.35% and 16.39%, respectively. However, the device based on the

M-PH1000 electrode exhibits a PCE of only 10.10%, which is notably lower than those of the devices based on Ag and M-PH1000@Ag electrodes due to the reduced conductivity and reflectivity. Considering the PV performances and stretchability of the corresponding electrodes, we believe that the M-PH1000@Ag electrode is promising to be used as an opaque electrode for high-performance stretchable OPVs.

2.3. Stretchable Transparent Electrode

We selected AgNWs as a stretchable transparent electrode. However, the fabrication of an AgNW transparent electrode with excellent optical and electrical performances using spin coating is challenging. Hence, it is crucial to develop a simple processing method that can yield a high-performance AgNW transparent electrode. In this regard, we developed a water SVA method to enhance the optical and electrical properties of AgNWs. A schematic of this method is shown in **Figure 5**a. The operation methods are presented in Experimental Section (Supporting Information). The function of the SVA treatment is to improve the wettability of the AgNW solution on the substrate via the large surface tension difference between ethanol and water molecules. As AgNWs are directly spin-coated on the electron transport layer (ZnO NPs) during the device fabrication, as shown in Figure S12 and Table S5 (Supporting Information), we measured the water-DIM contact angles of the ZnO NPs films with and without SVA treatment and calculated the surface energies of the corresponding films. The surface energy of the film without the SVA treatment was 48.1 mN m^{-1}. After the SVA treatment, the surface energy of the film was significantly increased to 63.0 mN m^{-1}, considerably closer to that of pure water (≈72 mN m^{-1}). Consequently, the higher-surface-energy film treated with SVA better wets the ethanol-dispersed AgNW solution (with a surface tension of ≈22.4 mN m^{-1}). According to the second law of thermodynamics, the transition from order to disorder is associated with an increase in entropy, and the disordered state or that without orientation is more energetically favorable. With the SVA treatment, the wetting behavior between the substrate and Ag NWs is enhanced, and the Gibbs free energy must decrease, which forms a strong force to freeze the Ag NWs in a disordered state and make them less affected by the shearing stress caused by the centrifugal force and fluid. Additionally, as shown in Figure 5b, we employed X-ray photoelectron spectroscopy (XPS) to confirm that the ethanol-dispersed AgNWs did not affect the ZnO NP layer upon spin coating. This ensures that the device remains undamaged during the AgNW spin coating.

To verify the effect of the SVA treatment on the morphologies of the AgNW films, we acquired scanning electron microscopy (SEM) images of AgNW films with and without SVA treatment. As shown in Figure S13 (Supporting Information), at large scan sizes (≈18 × 25 μm^2), the AgNW films without SVA treatment exhibited an inhomogeneous distribution. After the SVA treatment, the AgNW film was more uniformly dispersed. Further, as shown in Figure 5c,d, we scanned AgNW films with smaller sizes (≈3.5 × 5 μm^2). The AgNW films without SVA treatment exhibited a radial alignment. However, after the SVA treatment, the arrangement of AgNWs is more evenly distributed. As shown in Figure 5e,f, to quantitatively analyze the alignment behavior of the AgNW films, we analyzed the orientation degrees of the corresponding AgNW films by the software Image J (the coloring basis is shown in Figure S14, Supporting Information), and defined the main orientation direction of the AgNWs as 0°. As shown in Figure 5g, we plotted the distribution densities of the orientation angles of the AgNW films with and without SVA treatment. Without the SVA treatment, the proportion of AgNWs within 15° from the main alignment direction is as high as 55.8%, while, after the SVA treatment, the proportion of the corresponding area decreased to only 33.4%. This confirms that the SVA treatment has a significant influence on the alteration of the arrangement of AgNWs. Additionally, as shown in Figure S15 (Supporting Information), the same trend of the two Ag NW dispersions is observed in the optical microscopy images.

Subsequently, we measured the electrical and optical properties of AgNW films with and without SVA treatment. Regarding the electrical properties, as shown in Figure 5h, both films exhibited low sheet resistances (R_{sh} ≈ 6.5 Ω sq^{-1}) along the main alignment direction of AgNWs. However, there was a significant difference in R_{sh} in the direction perpendicular (90°) to the main alignment direction. R_{sh} of the AgNW film without SVA treatment in the 90° direction is almost twice that at 0°, while R_{sh} of the AgNW film is almost unchanged after the SVA treatment. Regarding the optical properties, as shown in Figure 5i, as the SVA treatment can make the AgNWs more uniform, the film with the SVA treatment exhibits a better optical transmittance than that without the SVA treatment. This improvement can be attributed to the SVA treatment, which facilitated a more uniform deposition and less ordered arrangement of AgNWs in the film. Consequently, these modifications resulted in enhanced optical and electrical properties.

Further, we fabricated rigid top-illuminated devices with a structure of glass/Ag/PCP-2F-Li/PEDOT:PSS/PM6:L8-BO/ZnO NPs/AgNWs to investigate the effects of these two types of AgNW transparent electrodes on the PV performance. As shown in Figure 5j and Table S4 (Supporting Information), the OPV based on the AgNW transparent electrode without SVA treatment delivers a PCE of 14.04%. The device based on the AgNW transparent electrode with the SVA treatment exhibits a high PCE of 16.39%, which is the best result among OPVs based on AgNWs as a top transparent electrode. The results demonstrate that the optimized optical and electrical properties of the transparent electrode could largely increase the PV performances of the devices.

2.4. Stretchable OPV Devices

Through the above stretchable performance optimization of the active layer, opaque electrode, and transparent electrode, considering the advantage that the performance of the top-illuminated device structure is independent on the optical performance of the substrate, we successfully integrated these stretchable functional layers on a TPU substrate to fabricate *is*-OPVs based on the top-illuminated structure (as shown in Figures 1a and 6a). The schematic diagram of the detailed preparation process of *is*-OPVs is shown in Figure S16 (Supporting Information). As shown in Figure 6c,d, we analyzed the PV performances of PM6:L8-BO blend films with different SEPS contents on stretchable substrates. **Table 2** summarizes the corresponding device

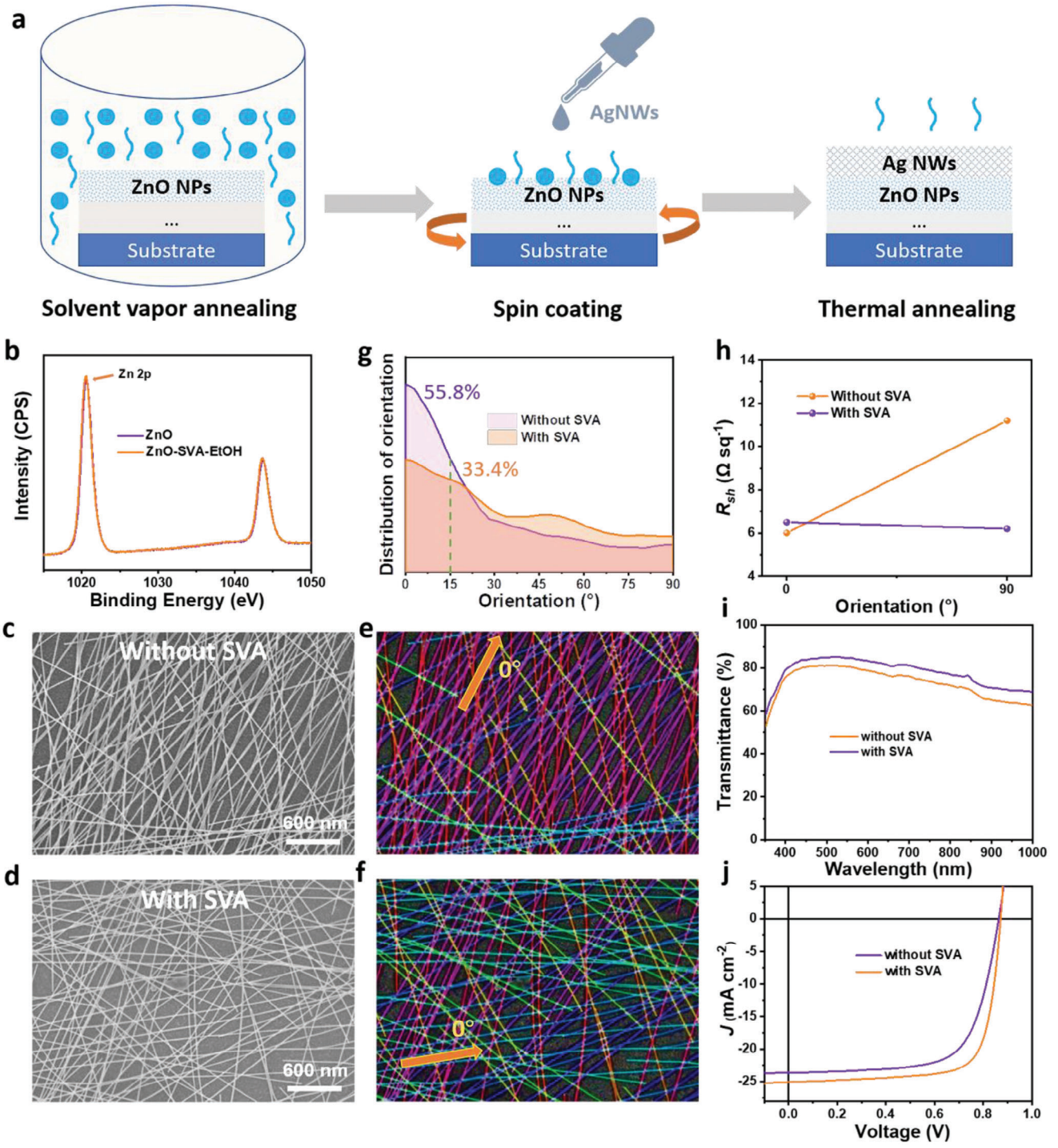

Figure 5. Stretchable transparent electrode. a) The schematic diagram of the SVA treatment: 1) placing the substrate coated with ZnO NPs in a Petri dish containing water vapor for SVA, which facilitates the formation of a layer of water vapor on the surface of ZnO NPs; 2) depositing the ethanol-dispersed AgNWs on ZnO NPs by spin-coating; 3) annealing the device to remove ethanol and moisture. b) The Zn 2p XPS spectra of ZnO NPs films with and without SVA treatment. The SEM images of AgNWs films without (c) and with (d) SVA treatment. The Image J analysis results for orientations in AgNWs films without (e) and with (f) SVA treatment. g) The distribution density of the orientation angles of AgNWs films with and without SVA treatment. h) The sheet resistance of AgNWs films with and without SVA treatment in 0° and 90° directions. i) The transmittance of AgNWs films with and without SVA treatment. j) The *J*–*V* curves of binary top-illuminated devices based on AgNWs transparent electrodes with and without SVA treatment.

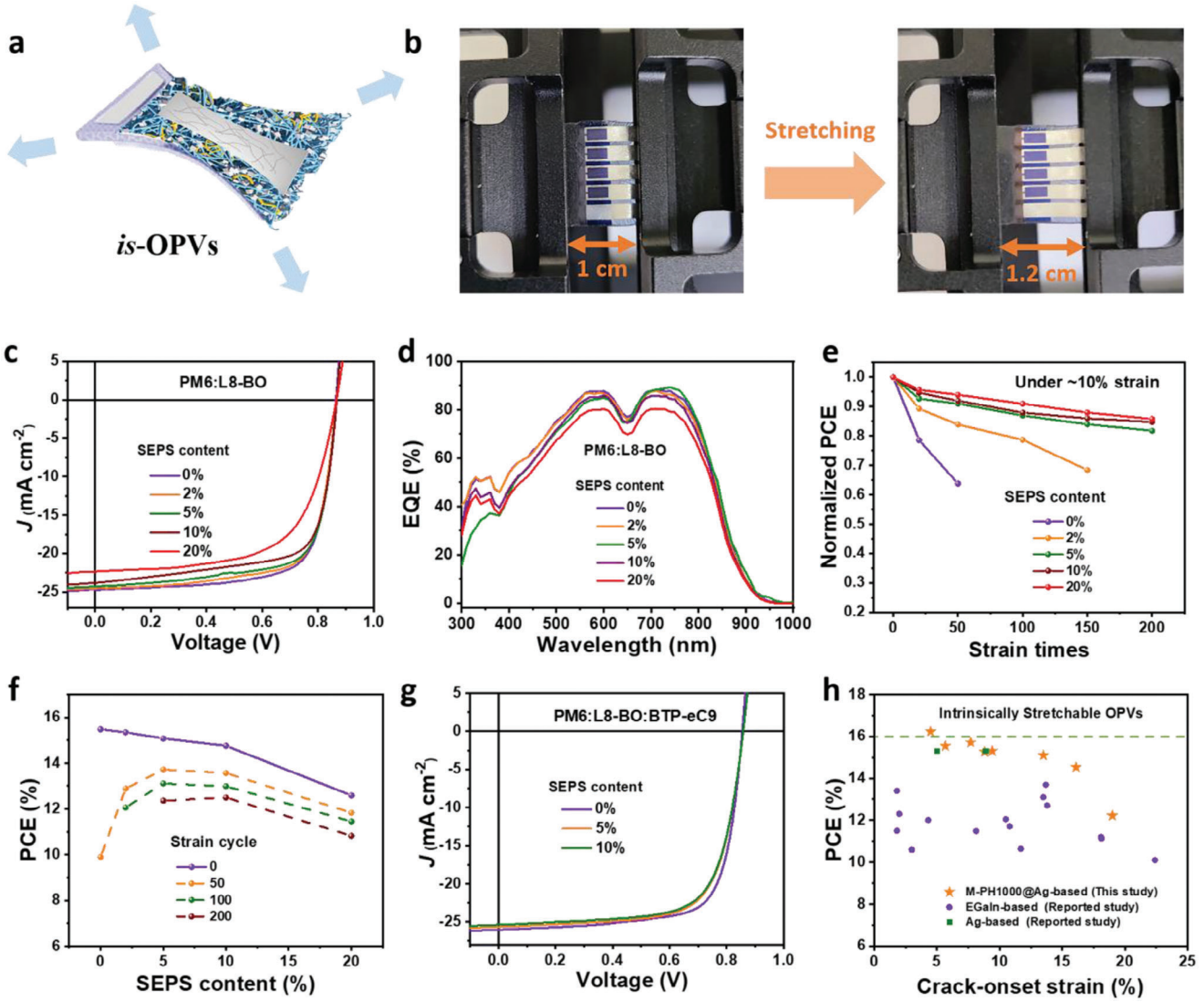

Figure 6. Stretchable OPV devices. a) Schematic diagram of *is*-OPVs. b) The pictures of the *is*-OPVs stretching process. c) *J*–*V* characteristics and d) EQE spectra of binary (PM6:L8-BO) *is*-OPVs with different SEPS contents. e) Normalized PCEs of the 10% strain-tested PM6:L8-BO-based *is*-OPV devices with different SEPS contents. f)The PCEs-SEPS contents curve with different stretching times of the *is*-OPVs. g) *J*–*V* characteristics of ternary (PM6:L8-BO:BTP-eC9) *is*-OPVs with different SEPS contents. h) Comparison of PCEs and COS in this work with those of *is*-OPVs reported in previous literature.

Table 2. Photovoltaic performances of the *is*-OPVs. The ± refers to the standard deviation.

	SEPS content	V_{OC} [V]	J_{SC} [mA cm^{-2}]	*FF* [%]	PCE [%]
PM6:L8-BO	0%	0.86	24.71	72.84	15.54 (15.17±0.19)
	2%	0.87	24.52	72.05	15.30 (14.96±0.21)
	5%	0.87	24.29	71.64	15.09 (14.75±0.17)
	10%	0.87	23.83	70.33	14.53 (14.19±0.18)
	20%	0.87	22.35	63.06	12.21 (11.97±0.15)
PM6:L8-BO:BTP-eC9	0%	0.86	26.05	72.86	16.23 (15.84±0.24)
	5%	0.86	25.67	71.40	15.71 (15.29±0.22)
	10%	0.86	25.37	70.25	15.26 (14.88±0.23)

parameters. The control PM6:L8-BO-based devices exhibit the best efficiency of 15.54%, among the highest PCEs for elastomer substrate-based OPVs. The *is*-OPV devices with 2%, 5%, 10%, and 20% SEPS deliver PCEs of 15.30%, 15.09%, 14.53%, and 12.21%, respectively, which are consistent with the performance variation of rigid indium tin oxide (ITO)-based devices.

The stretchability of *is*-OPVs is a key performance factor in practical applications, which strongly depends on the intrinsic stretchability of each layer and interfacial connection performance between two adjacent layers.[8] We conducted stretching tests on *is*-OPVs to analyze the impact of the addition of SEPS on their stretchability. Figure 6b shows that SEPS significantly improves the stretchability of the devices. Without SEPS, the PCE of the PM6:L8-BO binary device decreases to 63.8% after 50 stretch-release cycles at a stretching level of 10%, and the device is broken after 100 cycles. The addition of 2% SEPS slightly enhanced the stretchability; 68.4% of the PCE was retained after 150 cycles. As the stretching continued, the devices lost their PV behavior. Notably, when the SEPS content exceeded 5%, the device stretchability was improved significantly due to the formation of a continuous SEPS network in the active layer. The devices with 5%, 10%, and 20% SEPS retained 81.8%, 84.7%, and 86.0% of the PCEs after 200 stretch-release cycles at a stretching level of 10%, respectively, which highlights the advantage of SEPS in enhancing the device stretchability, and verifies the reliability of the electrodes and interface connections. Figure 6f presents SEPS content-PCE curves for different stretching cycles, which illustrate the variation in PV performance with the different SEPS contents and number of stretching cycles. The results indicate that the *is*-OPVs achieved the highest PCE retention when the SEPS content was 5–10% under a fixed stretching cycle, which demonstrates the optimal balance between the efficiency and stretchability for *is*-OPVs.

Moreover, following the approach employed for rigid ITO devices, we employed a ternary device strategy to further improve the performance of *is*-OPVs. The PV performances are shown in Figure 6g and Figure S17 (Supporting Information), while Table 2 summarizes the corresponding device parameters. The ternary blend PM6:L8-BO:BTP-eC9 with a stretchable architecture exhibits the best efficiency of 16.23%, which is the best result among stretchable substrate-based OPVs (statistical data are shown in Figure 6h and Table S6, Supporting Information). The ternary *is*-OPV devices with SEPS contents of 5% and 10% deliver PCEs of 15.71% and 15.26%, and can maintain 71.2% and 74.1% of the PCEs after 200 stretch-release cycles under 10% stretching (Figure S18, Supporting Information), respectively, consistent with the performance variation of binary PM6:L8-BO-based *is*-OPVs. Notably, the stretchability of ternary *is*-OPVs was lower than those of binary devices. This can be attributed to the increased crystallinity of the ternary active layer upon the addition of the highly crystalline BTP-eC9. As a result, the stretchability of the ternary blend films decreased, in line with the COS measurement results of the active layer (Tables S2 and S3, Supporting Information). In addition, to explore the device scaled-up capability of this *is*-OPVs, we fabricated a 1 cm^2 device based on PM6:L8-BO:BTP-eC9 blend films with 5% SEPS (the *J*–*V* curve is shown in Figure S19, Supporting Information). The 1 cm^2 *is*-OPVs delivers a PCE of 13.83%, with a V_{oc} of 0.84 V, a J_{sc} of 24.5 mA cm^{-2}, and an FF of 67.29%. And the 1 cm^2 device can maintain 68.1% of the PCE after 100 stretch-release cycles under 10% stretching (Figure S20, Supporting Information). It is also worth noting that the PCE of 1 cm^2 devices has inevitably declined compared to small-area devices. The main reason for the decreased performance is the resistance loss of the transparent electrode, and the softness of the TPU substrate presents processing challenges.[42] Nonetheless, this still proves that the stretchable electrodes and active layers we developed have the ability to up-scale the device area.

3. Conclusions

We developed an *is*-OPV device with a SEPS-containing active layer, AgNW transparent electrode, M-PH1000@Ag opaque electrode, and top-illumination structure, and demonstrated that the *is*-OPV device simultaneously delivered the merits of a high performance and good stretchability. First, the stretchability of the active layer was largely increased by adding a low-elastic-modulus elastomer, i.e., SEPS, with a slight device performance degradation trend. Second, the stretchability and conductivity of the opaque electrode were enhanced by a conductive polymer/metal (M-PH1000@Ag) composite electrode strategy, which maximized the stretchability and electrical performance of the opaque electrode. Third, the optical and electrical properties of the AgNW transparent electrodes were improved by the SVA strategy. Notably, through the thorough optimizations, the *is*-OPVs exhibited a high efficiency of 16.23%, which is the best value among *is*-OPVs. In addition, the stretchable OPVs achieved a balance of efficiency and stretchability with SEPS elastomer contents of 5–10%. Overall, our study demonstrates a very promising *is*-OPV structure for practical applications.

Supporting Information

Supporting Information is available from the Wiley Online Library or from the author.

Acknowledgements

X.Z., X.W., and Q.W. contributed equally to this work. L.Z., M.S., and H.C. thank the support from the National Natural Science Foundation of China (Nos. 52127806, 52173185, 22279114, and 61721005), National Key Research and Development program of China (Nos. 2019YFA0705902), the S&T Innovation 2025 Major Special Program of Ningbo (No. 2018B10055), the Research Startup Fund from Zhejiang University, and the Fundamental Research Funds for the Central Universities (No.226-2022-00133, 226-2023-00113). W.M. and Q.W. thank the support from the National Key Research and Development Program of China (2022YFE0132400), the NSFC (21875182 and 52173023), Key Scientific and Technological Innovation Team Project of Shaanxi Province (2020TD-002), and 111 project 2.0 (BP0618008) and China National Postdoctoral Program for Innovative Talent Support under Grant BX20220249. Q. L. and C. M. thank the support from the Youth Innovation Promotion Association of CAS (2019317).

Conflict of Interest

The authors declare no conflict of interest.

Author Contributions

X.Z. and L.Z. developed the concept and designed the experiments. L.Z., M.S., and H.C. supervised the project. X.Z. and X.W. performed OPVs fabrication and characterization. W.F. patterned M-PH1000@Ag electrode. Y.H., Q.L., and C.M. synthesized ZnO NPs. Q.W. performed COS measurements. J.X., G.D., and W.M. performed GIWAXS measurements. T.C. and Y.K. performed AFM measurements. M.W and Y.W. performed contact angle measurements. Y.Z. performed SEM measurements. X.Z., L.Z., M.S., and H.C. analyzed the results and prepared the manuscript. All authors commented on the manuscript.

Data Availability Statement

The data that support the findings of this study are available from the corresponding author upon reasonable request.

Keywords

AgNWs transparent electrode, composite electrode, ITO-free devices, stretchable organic photovoltaics, top-illuminated devices

Received: July 22, 2023
Revised: November 27, 2023
Published online: December 24, 2023

[1] S. Park, S. W. Heo, W. Lee, D. Inoue, Z. Jiang, K. Yu, H. Jinno, D. Hashizume, M. Sekino, T. Yokota, K. Fukuda, K. Tajima, T. Someya, *Nature* **2018**, *561*, 516.
[2] G. Chen, X. Xiao, X. Zhao, T. Tat, M. Bick, J. Chen, *Chem. Rev.* **2022**, *122*, 3259.
[3] X. Zheng, L. Zuo, K. Yan, S. Shan, T. Chen, G. Ding, B. Xu, X. Yang, J. Hou, M. Shi, H. Chen, *Energy Environ. Sci.* **2023**, *16*, 2284.
[4] X. Zheng, L. Zuo, F. Zhao, Y. Li, T. Chen, S. Shan, K. Yan, Y. Pan, B. Xu, C.-Z. Li, M. Shi, J. Hou, H. Chen, *Adv. Mater.* **2022**, *34*, 2200044.
[5] J. Huang, Z. Lu, J. He, H. Hu, Q. Liang, K. Liu, Z. Ren, Y. Zhang, H. Yu, Z. Zheng, G. Li, *Energy Environ. Sci.* **2023**, *16*, 1251.
[6] D. Lv, Q. Jiang, D. Liu, *Solar RRL* **2023**, 2300234.
[7] H. Jinno, T. Yokota, M. Koizumi, W. Yukita, M. Saito, I. Osaka, K. Fukuda, T. Someya, *Nat. Commun.* **2021**, *12*, 2234.
[8] J. S. Park, G.-U. Kim, S. Lee, J.-W. Lee, S. Li, J.-Y. Lee, B. J. Kim, *Adv. Mater.* **2022**, *34*, 2201623.
[9] Y. Liu, B. Liu, C.-Q. Ma, F. Huang, G. Feng, H. Chen, J. Hou, L. Yan, Q. Wei, Q. Luo, Q. Bao, W. Ma, W. Liu, W. Li, X. Wan, X. Hu, Y. Han, Y. Li, Y. Zhou, Y. Zou, Y. Chen, Y. Liu, L. Meng, Y. Li, Y. Chen, Z. Tang, Z. Hu, Z.-G. Zhang, Z. Bo, *Sci China Chem* **2022**, *65*, 1457.
[10] Z. Zheng, J. Wang, P. Bi, J. Ren, Y. Wang, Y. Yang, X. Liu, S. Zhang, J. Hou, *Joule* **2022**, *6*, 171.
[11] Y. Jiang, X. Dong, L. Sun, T. Liu, F. Qin, C. Xie, P. Jiang, L. Hu, X. Lu, X. Zhou, W. Meng, N. Li, C. J. Brabec, Y. Zhou, *Nat. Energy* **2022**, *7*, 352.
[12] L. Zhu, M. Zhang, J. Xu, C. Li, J. Yan, G. Zhou, W. Zhong, T. Hao, J. Song, X. Xue, Z. Zhou, R. Zeng, H. Zhu, C.-C. Chen, R. C. I. Mackenzie, Y. Zou, J. Nelson, Y. Zhang, Y. Sun, F. Liu, *Nat. Mater.* **2022**, *21*, 656.
[13] S. Guan, Y. Li, K. Yan, W. Fu, L. Zuo, H. Chen, *Adv. Mater.* **2022**, *34*, 2205844.
[14] C. Li, J. Zhou, J. Song, J. Xu, H. Zhang, X. Zhang, J. Guo, L. Zhu, D. Wei, G. Han, J. Min, Y. Zhang, Z. Xie, Y. Yi, H. Yan, F. Gao, F. Liu, Y. Sun, *Nat. Energy* **2021**, *6*, 605.
[15] L. Zhan, S. Yin, Y. Li, S. Li, T. Chen, R. Sun, J. Min, G. Zhou, H. Zhu, Y. Chen, J. Fang, C.-Q. Ma, X. Xia, X. Lu, H. Qiu, W. Fu, H. Chen, *Adv. Mater.* **2022**, *34*, 2206269.
[16] L. Zuo, S. B. Jo, Y. Li, Y. Meng, R. J. Stoddard, Y. Liu, F. Lin, X. Shi, F. Liu, H. W. Hillhouse, D. S. Ginger, H. Chen, A. K.-Y. Jen, *Nat. Nanotechnol.* **2022**, *17*, 53.
[17] G. Ding, T. Chen, M. Wang, X. Xia, C. He, X. Zheng, Y. Li, D. Zhou, X. Lu, L. Zuo, Z. Xu, H. Chen, *Nano-micro. Lett.* **2023**, *15*, 92.
[18] Q. Wu, Y. Yu, X. Xia, Y. Gao, T. Wang, R. Sun, J. Guo, S. Wang, G. Xie, X. Lu, E. Zhou, J. Min, *Joule* **2022**, *6*, 2138.
[19] Y. Han, Z. Hu, W. Zha, X. Chen, L. Yin, J. Guo, Z. Li, Q. Luo, W. Su, C.-Q. Ma, *Adv. Mater.* **2022**, *34*, 2110276.
[20] Q. Wu, W. Wang, Y. Wu, R. Sun, J. Guo, M. Shi, J. Min, *Natl Sci Rev* **2022**, *9*, 151.
[21] L. Zhang, B. Lin, B. Hu, X. Xu, W. Ma, *Adv. Mater.* **2018**, *30*, 1800343.
[22] H. B. Naveed, W. Ma, *Joule* **2018**, *2*, 621.
[23] Y. Li, Y. Guo, Z. Chen, L. Zhan, C. He, Z. Bi, N. Yao, S. Li, G. Zhou, Y. Yi, Y. M. Yang, H. Zhu, W. Ma, F. Gao, F. Zhang, L. Zuo, H. Chen, *Energy Environ. Sci.* **2022**, *15*, 855.
[24] C. He, Y. Pan, Y. Ouyang, Q. Shen, Y. Gao, K. Yan, J. Fang, Y. Chen, C.-Q. Ma, J. Min, C. Zhang, L. Zuo, H. Chen, *Energy Environ. Sci.* **2022**, *15*, 2537.
[25] L. Zhan, S. Li, Y. Li, R. Sun, J. Min, Z. Bi, W. Ma, Z. Chen, G. Zhou, H. Zhu, M. Shi, L. Zuo, H. Chen, *Joule* **2022**, *6*, 662.
[26] T. Chen, S. Li, Y. Li, Z. Chen, H. Wu, Y. Lin, Y. Gao, M. Wang, G. Ding, J. Min, Z. Ma, H. Zhu, L. Zuo, H. Chen, *Adv. Mater.* **2023**, *35*, 2300400.
[27] J. Wang, Z. Zheng, P. Bi, Z. Chen, Y. Wang, X. Liu, S. Zhang, X. Hao, M. Zhang, Y. Li, J. Hou, *Natl Sci Rev* **2023**, *10*, nwad085.
[28] B. Parida, S. Iniyan, R. Goic, *Renew. Sust. Energ. Rev.* **2011**, *15*, 1625.
[29] N. Cui, Y. Song, C.-H. Tan, K. Zhang, X. Yang, S. Dong, B. Xie, F. Huang, *Npj Flex Electron* **2021**, *5*, 31.
[30] Q. Wan, S. Seo, S.-W. Lee, J. Lee, H. Jeon, T.-S. Kim, B. J. Kim, B. C. Thompson, *J. Am. Chem. Soc.* **2023**, *145*, 11914.
[31] S. Seo, J.-W. Lee, D. J. Kim, D. Lee, T. N.-L. Phan, J. Park, Z. Tan, S. Cho, T.-S. Kim, B. J. Kim, *Adv. Mater.* **2023**, *35*, 2300230.
[32] J.-W. Lee, C. Lim, S.-W. Lee, Y. Jeon, S. Lee, T.-S. Kim, J.-Y. Lee, B. J. Kim, *Adv. Energy Mater.* **2022**, *12*, 2202224.
[33] J.-W. Lee, S. Seo, S.-W. Lee, G.-U. Kim, S. Han, T. N.-L. Phan, S. Lee, S. Li, T.-S. Kim, J.-Y. Lee, B. J. Kim, *Adv. Mater.* **2022**, *34*, 2207544.
[34] J.-W. Lee, C. Sun, S.-W. Lee, G.-U. Kim, S. Li, C. Wang, T.-S. Kim, Y.-H. Kim, B. J. Kim, *Energy Environ. Sci.* **2022**, *15*, 4672.
[35] J.-W. Lee, G.-U. Kim, D. J. Kim, Y. Jeon, S. Li, T.-S. Kim, J.-Y. Lee, B. J. Kim, *Adv. Energy Mater.* **2022**, *12*, 2200887.
[36] Z. Peng, K. Xian, J. Liu, Y. Zhang, X. Sun, W. Zhao, Y. Deng, X. Li, C. Yang, F. Bian, Y. Geng, L. Ye, *Adv. Mater.* **2023**, *35*, 2207884.
[37] J. Liu, J. Deng, Y. Zhu, X. Geng, L. Zhang, S. Y. Jeong, D. Zhou, H. Y. Woo, D. Chen, F. Wu, L. Chen, *Adv. Mater.* **2023**, *35*, 2208008.
[38] Z. Peng, K. Xian, Y. Cui, Q. Qi, J. Liu, Y. Xu, Y. Chai, C. Yang, J. Hou, Y. Geng, L. Ye, *Adv. Mater.* **2021**, *33*, 2106732.
[39] W. Song, K. Yu, J. Ge, L. Xie, R. Zhou, R. Peng, X. Zhang, M. Yang, Z. Wei, Z. Ge, *Matter* **2022**, *5*, 1877.
[40] Z. Wang, D. Zhang, M. Xu, J. Liu, J. He, L. Yang, Z. Li, Y. Gao, M. Shao, *Small* **2022**, *18*, 2201589.
[41] L. Zuo, S. Zhang, H. Li, H. Chen, *Adv. Mater.* **2015**, *27*, 6983.

[42] J. Huang, Z. Ren, Y. Zhang, K. Liu, H. Zhang, H. Tang, C. Yan, Z. Zheng, G. Li, *Adv. Funct. Mater.* **2021**, *31*, 2010172.
[43] Z. Wang, M. Xu, Z. Li, Y. Gao, L. Yang, D. Zhang, M. Shao, *Adv. Funct. Mater.* **2021**, *31*, 2103534.
[44] G. Zeng, W. Chen, X. Chen, Y. Hu, Y. Chen, B. Zhang, H. Chen, W. Sun, Y. Shen, Y. Li, F. Yan, Y. Li, *J. Am. Chem. Soc.* **2022**, *144*, 8658.
[45] Y. Sun, M. Chang, L. Meng, X. Wan, H. Gao, Y. Zhang, K. Zhao, Z. Sun, C. Li, S. Liu, H. Wang, J. Liang, Y. Chen, *Nat. Electron.* **2019**, *2*, 513.
[46] H.-Y. Hou, Y.-F. Zhang, J.-D. Chen, H.-M. Liu, H. Ren, Y.-Q. Li, H. Mao, J.-X. Tang, *Chem. Eng. J.* **2022**, *450*, 138181.
[47] C. Xie, Y. Liu, W. Wei, Y. Zhou, *Adv. Funct. Mater.* **2022**, *33*, 2210675.
[48] Y. Kong, Y. Li, G. Hu, N. Cao, Y. Ling, D. Pan, Q. Shao, Z. Guo, *Polym. Adv. Technol.* **2018**, *29*, 2344.